Volume 1 | Number 1 | Jan 2013 | Pages 1–100

Journal of
Materials Chemistry C

Materials for optical and electronic devices
www.rsc.org/materialsC

ROYAL SOCIETY
OF CHEMISTRY

ROYAL SOCIETY
OF CHEMISTRY

www.rsc.org/materialsC

Preparation of multi-layer graphene on nickel coated silicon microchannel plates by hydrothermal carbonization procedure and its improved field emission properties

Dajun Wu[a], Chi Zhang[a], Cheng Liang[a], Yiping Zhu[a*], Shaohui Xu[a,b], Dayuan Xiong[a], Shaolin Xue[c], Lianwei Wang[a,b*], Paul K. Chu[b]

[a] Key Laboratory of Polar Materials and Devices, Ministry of Education, and Department of Electronic Engineering, East China Normal University, 500 Dongchuan Road, Shanghai 200241, P. R. China

[b] Department of Physics and Material Science, City University of Hong Kong, Tat Chee Avenue, Kowloon, Hong Kong, China

[c] College of Science, Donghua University, Shanghai 201620, P. R. China

*Corresponding author:

Yiping Zhu (Tel:+86-21-54342501; Fax: +86-21-54345119; Email: ypzhu@ee.ecnu.edu.cn)

Lianwei Wang (Tel: +86-21-54345160; Fax: +86-21-54345119; Email: lwwang@ee.ecnu.edu.cn)

1

Abstract

An emission cell comprising multi-layer graphene (MLG) on nickel-coated silicon microchannel plates (Ni/Si-MCPs) was prepared.   The Ni_3C film was formed on the Si-MCPs by hydrothermal carburization in a polyol solution containing a small amount of NaAc as the carbon source and thermal annealing was performed to produce the vertically and horizontally aligned multi-layer graphene field-emission cathode on the surface of the Ni/Si-MCPs (MLG-MCPs).   The microstructure and surface morphology was investigated and field emission (FE) studies indicated that the MLG-MCPs delivered better FE performance than Ni/Si-MCPs, which contributed to the characteristic of had sharp edges, large aspect ratio, and the vertically and horizontally aligned and patterned MLG with good electrical conductivity.   The turn-on field of the sample annealed at 800 ^{o}C was 2.0 V/μm at a current density of 10 μA/cm^2 and the field emission threshold was 3.2 V/μm at 1 mA/cm^2.   The structure was very stable showing 97.5% retention after continuous operation for over 6 h at 2×10^{-5} Pa, suggesting a promising candidate for FE devices. This would open up possibilities for the next generation FE electron sources from well-aligned macroporous graphene with skeleton and extend their practical applications.

1. Introduction

Synthesis and application of carbon materials such as active carbon,[1] fullerene,[2] carbon nanotubes,[3] and graphene[4] have been extensively studied because of potential

applications in energy storage, solar cells, sensors, catalysts and electron-emission displays.[5]   Since the first demonstration of electron field emission (FE) from carbon nanotubes (CNTs),[3] carbon-based cold cathodes including nanotubes,[6] graphene,[7] and graphite flakes[8] have garnered much attention as potential emitters in field emission displays (FEDs).   In particular, graphene,[4] a single sheet of sp^2-bonded carbon atoms in a honeycomb crystal lattice, has unique electronic properties and crystal structure suitable for future electronic structures such as nanoelectronic devices, touch screens, transparent electrodes, and field-emission displays (FEDs).   Graphene and graphene-based hybrid structures have been shown to have excellent cold cathode field-emission characteristics due to the large aspect ratio, sharp edges, excellent electrical property, and physical/chemical stability.[9,10]   For example, Wu et al. demonstrated that single-layer graphene deposited by electrophoresis had outstanding field emission properties.[11]   Moreover, the FE properties of many types of graphene sheets such as single-layer graphene films[11], graphene composite films[12], vertically aligned few-layer graphene (FLG) sheets[13], and multi-layer graphene films (MLG) sheets[14] had been demonstrated to be similar to or even better than common carbon materials such as carbon nanotubes (CNT).   Du et al.[12] exploited the edge effect to enhance field emission from graphene films by creating topographic structures with more edges on a microprobe equipped in a scanning electron microscopy (SEM). Kaushik et al.[14] reported improved field emission from graphene films grafted with metal nanoparticles and the turn-on and threshold fields decreased with grafting of Ti, Pd, Ag, and Au.   Other graphene-based hybrid structures encompassing metals,

CNTs, oxides, and halides have also been studied in order to reduce the work function and increase field emission.[15,16] For example, Xu et al.[23] synthesized grass-like ZnSe nanostructures on graphene oxide hydrothermally and the materials possess good field-emission properties including a low turn-on field of 4.5 V μm^{-1} and high field enhancement factor of 2715. Besides, vertical, aligned and dense sharp edges on a given substrate provide an attractive solution to obtain excellent FE properties. Usually, the well-aligned graphene arrays were designed to fabricate low turn-on electric field and excellent stability. Recently much attention had been paid to the preparation of patterned and aligned graphene films[19-21] and graphene-based hybrid structures to reduce the turn-on field and increase the current density using processes compatible with integrated circuit (IC) processing. Vertically aligned graphene field-emission structures were fabricated by electrophoretic deposition (EPD) and photolithography of CNTs with SU-8 photoresist and Peng et al.[19] fabricated patterned reduced graphene oxide nano-sheets (rGOs) on conductive silicon with a turn-on field of 3.34 V/μm at 10μA/cm^2. Deng et al.[20] produced vertically aligned multi-layer graphene-silicon nanowires (MLG-SiNWs) with a low turn-on electric field of 2.42 V/μm and good FE stability, and that Huang and co-works[21] reported that the turn-on electric field of their patterned graphene film was 7.2 V/μm at 100 nA/cm^2. However, the preparation method of CVD is poor efficiency, and high cost, then Hummers method is not environment-friendly. Herein, the nickel-coated silicon microchannel plates (Ni/Si-MCPs) were employed as the template to form multi-layer graphene on nickel-coated silicon microchannel plates (MLG-MCPs) by hydrothermal

carbonization procedure.　The well-aligned MLG-MCPs was composed of a 6×6 μm

pore array about 250 μm deep and 1 μm thick and after annealing, multi-layer

graphene was formed on the surface and inner sidewall of the Ni/Si-MCPs.　The

field-emission properties of the MLG-MCPs such as the turn-on field, threshold, and

stability are better than those of many patterned graphene structures reported

previously.[19-21]


2.　Experimental section

2.1.　Materials

All chemical reagents were AnalaR (AR) grade and used as received without

further purification. Sodium acetate （$Na_2C_2O_4$）, nickel chloride ($NiCl_2 \cdot 6H_2O$),

ammonium chloride (NH_4Cl), ethanol, sodium hypophosphite ($NaH_2PO_2 \cdot H_2O$),

acetone and all of the other reagents were purchased from Aladdin Reagent.

Triethylene glycol (TEG)($C_6H_{14}O_4$) was purchased from Sinopharm Chemical

Reagent Co. Ltd.　The aqueous solutions were performed by 18 MΩ deionized water.

Corundum (2000 mesh) and metal polishing agent was purchased from

Hinomoto Kenmazai Co. Ltd.

2.2.　Preparation of Ni/Si-MCPs.

Si-MCPs were fabricated by a single step of photo-assisted electrochemical

etching for p-type silicon, which were based on our co-workers' work in Refs.[38, 39]

The square array with channels about 250 μm deep had 6×6 μm pores and 1 μm thick

wall with an intrinsic resistance on the order of kΩ.

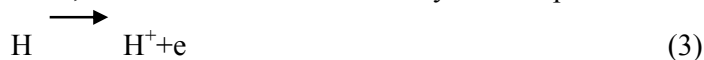In an acidic nickel electroless plating bath, reduction of the silicon atoms will

firstly yield atomic hydrogen.[46]

$$Si+ 2OH^- +H_2O \longrightarrow SiO_3^{2-} +4H \qquad (1)$$
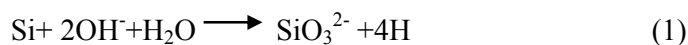
Among atomic hydrogen, a part of them recombine to form hydrogen.

$$H+H \longrightarrow H_2 \qquad\qquad (2)$$

Then, the nickel ions are reduced by another part of atomic hydrogen.

$$H \longrightarrow H^+ + e \qquad\qquad (3)$$

$$Ni^{2+} + 2e \longrightarrow Ni \qquad\qquad (4)$$

So, the balls were deposited on surface and inner side walls of the prepared Si-MCPs by the method of liquid flow to form Ni/Si-MCPs.

Electroless deposition of the porous nano-Ni films and balls were performed in a plating bath.　5.0g NH_4Cl and 1.2g $NaH_2PO_2·H_2O$ were dissolved in 90 ml 24 mM $NiCl_2·6H_2O$ solution to form green mixture.　The PH of resulting solution was changed 9 to 11 by NH_4OH and stirred for 30 min.　Then, the access solution heated to 90℃ and stirred vigorously.　Si-MCPs were immersed into the HF mix-solution (HF: C_2H_5OH: H_2O, 100: 125: 10, V/V) to etch nature 4nm SiO_2 layer of Si-MCPs. The washed Si-MCPs were transferred into electroless plating solution and stirred by magnetic stirring apparatus for 30 min at 90 ℃ in a liquid flow equipment.　The samples were dried at 80℃ overnight in a vacuum oven before carburization process.

2.3.　Preparation of MLG-MCPs.

1ml 1M sodium oxalate was dissolved in 20ml Triethylene glycol (TEG) to form mixture solution and stirred for 30 min. The as-prepared Ni/Si-MCPs were immersed in the 1% Triton X100 solution for 5 min to flush out the air of inner of Ni/Si-MCPs. Then, The Ni/Si-MCPs were introduced into the above mixture solution to finally form precursor solution, which was transferred into a 25 ml the Teflon-sealed stainless steel autoclave and sealed tightly.　Keeping the autoclave at　260℃ for 1 to 24 h finally led to the formation of carbon-incorporated Ni (Ni_3C)/Ni/Si-MCPs.　After that, the autoclave was allowed to cool down naturally. The samples of Ni_3C/Ni/Si-MCPs were washed with absolute ethyl alcohol and de-ionized water three times respectively, and at last dried at 80 ℃ overnight in a vacuum oven.　The hydrothermal products were placed in a tube furnace at 300℃ to 800℃ and annealed in an argon atmosphere for 30 min, resulting in MLG-coated nano-Ni films and balls in the inner wall and outer of Si-MCP(MLG-MCPs). (Sample 0: MLG-MCPs

550,annealed 550℃; Sample 1: MLG-MCPs 600, annealed 600℃; Sample 2: MLG-MCPs 700,annealed 700℃; Sample 3: MLG-MCPs 800;annealed 800℃).

2.4. Material Characterizations.

The morphologies, size and structures of the materials were investigated and characterized using various physiochemical techniques, including XRD, XPS, field emission scanning electron microscopy, Raman spectra analysis. The morphology and microstructure of MLG-MCPs were investigated by field-emission scanning electron microscopy (FE-SEM, Hitachi S-4800, Japan) and a high-resolution transmission electron microscope (HRTEM; Philips Tecanai G2 F30). The crystal structure and phase changes of samples during polyol treatment and high-temperature annealing were determined by X-ray diffraction (XRD, Rigaku, RINR2000, Japan). The layer thickness and structure of the MLG-MCPs were observed using mciro-Raman system (T6400 Jobin Yvon triple monochromator, Tokyo, Japan) facilitated with a charged coupled device detector with Ar ion 633nm laser. Carbon content in the $Ni_3C/Ni/Si$-MCPs was carried out with integrating the diffraction area for each phase from the XRD patterns before post-annealing.

2.5. Field Emission Measurements.

The field emission characteristics of MLG-MCPs were measured with the diode structure in a ball-type vacuum chamber at a pressure of $\sim2\times10^{-5}$ Pa. A schematic set up of electron-field-emission from MLG-MCP was showed in Figure 6a. The MLG-MCP emitters and a phosphor-coated indium-tin oxide (ITO) glass were used as the cathode and anode, respectively. Field emission current was measured as a function of supplied high positive voltage (Keithley 248) at the anode by a current meter (Keithley 6482 Picoammeters). In the measurements, the distance between electrodes (d) was remained ~500 μm. The electric field (E) was estimated by

dividing the applied voltage (V) by the sample-anode separation (E=V/d). Emission current density was determined by dividing current with the area of the sample exposed to the anode.   The measurements were carried out by continuously varying the anode voltage under two repeat cycles by increasing or decreasing the voltage between 500 V and 2800 V and their average was taken.   The samples of the MLG-MCPs were pre-emitted (2-3 cycles of measurements) before actual measurements.   In order to analyze the Field Emission behavior, the turn-on field (E_{to}) and the threshold field (E_{th}) were defined as the electric fields required to lead to a current density of $10 \mu A/cm^2$ and $1 mA/cm^2$, respectively.

3.   Results and discussion

The MLG was prepared on Ni/Si-MCP by hydrothermal carburization in a polyol solution containing a small amount of NaAc as the carbon source and afterwards, annealing was performed to form the multi-layer graphene.   As described in Fig. 1, p-type silicon was processed by one-step photo-assisted electrochemical etching (Fig. 1a) and nano-porous nickel balls and layers were deposited by electroless plating on the outer wall of the Si-MCPs (Fig. 1b).   Carburization was conducted at 260 ^{o}C for 6 h to produce carbon-incorporated Ni (Ni_3C)/Si-MCPs in a polyol solution containing the Na catalyst (Fig. 1c).   The multi-layer graphene (MLG) structure, MLG coated on Ni/Si-MCPs (MLG-MCPs), was then formed during annealing at 300~800 ^{o}C for 30 min under Ar atmosphere (Figs. 1d and 1e).

The SEM images of the as-synthesized highly ordered 3D high-aspect-ratio the template Si-MCPs are presented in Fig. 2a and 2b.   It can be seen that the Ni/Si-MCPs not only retained the original highly ordered 3D morphology (Fig. 2c and

d), but also the nickel current collector had good uniformity and high-aspect-ratio because of silicon assisted nickel electroless plating reaction.   The inset shows that the nickel current collector was composed of porous nickel balls with a diameter of about 50 nm, and that increased the surface activity of the nickel particles with sharp edges (Fig. 2c and Fig. 4b).   So, the carbon-incorporated Ni (Ni_3C)/Ni/Si-MCPs kept the original 3D morphology of the Ni/Si-MCPs (Fig. 3a) after hydrothermal carbonization because the morphology of Ni/Si-MCPs was not changed at 260 ℃. Compared to the Ni_3C/Si-MCPs, the ripples and wrinkles of MLG were observed (Fig. 3b), and that the MLG-MCPs inherited the original morphology from Ni_3C/Ni/Si-MCPs for lower thermal annealing (<1000 ℃).   The MLG-MCPs consists of carbon, oxygen, nickel, and silicon were shown in energy-dispersive spectrometry (EDS) of Fig. 3d.   The mass and atom ratios of carbon to the other elements were 19.5% and 47.3%, respectively, illustrating that the carbon-incorporated Ni/Si-MCPs was successfully synthesized by hydrothermal carburization.   After post-annealing, The MLG-MCPs was synthesized on the surface of Ni with sharp edges, large-aspect-ratio, and porosity, which should benefit field emission similar to that observed from Ni-assisted CVD materials.[22]

More detailed structural information and morphology evolution of the Ni_3C and MLG were investigated by TEM and selected area electron diffraction (SAED). HR-TEM images indicate that Ni_3C crystalline with 0.24 nm lattice spacing were found on the Ni with 0.2 nm lattice spacing, as shown in Fig. 4a and b; on the contrary, clear graphitic layers with 0.32 nm lattice spacing formed on the Ni surface after

post-annealing (Fig. 4c and d).   The MLG flakes consisted of areas, which were

rippled and wrinkled which was typical for graphene sheets due to their extreme

thinness and thermodynamic nature.   Consistent with the SEM observations, the

morphology of MLG such as sharp edges and defects were also formed because

silicon assisted nickel electroless plating reaction with sharp edges (Fig. 2c) and

thermal exfoliation (Fig. 5d), which is beneficial for the field emission.[14,15]   The

SAED pattern included a six fold symmetry diffraction dots illustrating the high

crystalline quality of the individual MLG.[16]   These results show that carbon atoms

that diffused into the Ni during the hydrothermal carburization process segregated and

exfoliated out to form MLG on the surfaces and inner of the Ni/MCPs by the

post-annealing.   The C 1s XPS spectra of the Ni_3C/Ni and MLG/Ni are shown in Fig.

4e and 4f.   The Ni_3C, Ni_xC, Csp^2, Csp^3, C-O, and C-OO related peaks were assigned

at 281.5, 283.3, 284.8, 285.3, 286.6, and 288.5 eV, respectively.[29]   It can be seen that

the Ni_xC and Ni_3C related peaks were disappeared to form carbon segregation on the

Ni balls after thermal annealing, and that these extra sp^3 sites will facilitate to the field

emission (Fig. 4f).

In order to study the hydrothermal carburization process of Ni/Si-MCPs in the

polyol solution, the phase changes in the samples were monitored by conducing X-ray

diffraction (XRD) on Ni/Si-MCPs, Ni_3C/Si-MCPs and MLG-MCPs, as shown in Fig.

5(a).   The starting Ni/Si-MCPs exhibited three peaks (marked with a pentagram)

attributed to the cubic phase Ni metal [JCPDS 70-1849 with the strongest peak (111)

at $2\theta = 44.8$, (200) peak at $2\theta = 52.3$, and (220) peak at $2\theta = 76.1$] and Si substrate

[(400), marked with triangle].   After hydrothermal carburization for 1 h, a new phase

(marked with diamond) with eight peaks appear from Ni/Si-MCP and can be ascribed

to the hexagonal nickel carbide (Ni_3C) (JCPDS 77-0194) which is consistent with the

before report of Ni_3C ((312) peak at 2θ=44.6, (212) peak at 2θ=39.1, (411) peak at

2θ=41.6, (611) peak at 2θ=58.4, (433) peak at 2θ=71.0, (314) peak at 2θ=78.0, (812)

peak at 2θ=85.7, (434) peak at 2θ=88.0),[22] indicating carbon permeated into the Ni

nanoparticles.   According to the Scherer equation, the average crystallite size of

Ni_3C ware estimated to be 40 nm, which was consistent with the characterizations of

TEM and SEM.

With the hydrothermal carburization time increased from 1 to 9 h, the diffraction

peak intensity of the cubic phase nickel gradually decreased, while the hexagonal

nickel carbide peak intensity apparently increased.   After 9 h of hydrothermal

carburization, the cubic phase nickel peak finally attained to be minimizing, then the

Ni_3C phase reached to a peak value 4.51wt%, which indicated that the nickel

nano-sheets and balls of Ni/Si-MCPs were converted into nickel carbide nanoparticles

by the hydrothermal carburization process in polyol solution.   For quantitative

calculation of the carbon content in the Ni_3C/Si-MCPs, we integrated the X-ray

diffraction patterns area for each phase.   Fig. 5b illustrated carbon content of the

Ni_3C/Si-MCPs as a function of the hydrothermal polyol carburization time, and the

carbon content increased linearly for the first 6 h of hydrothermal polyol carburization

and has led to be maximized at 4.51 wt% after 9 h of carburization, which was lower

than the stoichiometric carbon content in Ni_3C of 6.39 wt%.   The reasons are porous

nickel layers are composed of cross connection-nanoballs deposited on surface and inner side walls of the prepared Si-MCPs, which lead to few zone of nickel are not absolutely exposed to the polyol solution, resulting in fault of local carburization. However, the nickel particles with diameter of about 50 nm can enhance contact area between nickel and polyol solution, developing the carbon content of Ni_3C/Si-MCPs. These results clearly illustrate that the as-prepared Ni/Si-MCPs reacted with polyol to effectively induce the cleavage of the C-C bonds of polyol, so dissociating it into carbon segment that diffused into the Ni/Si-MCPs, leading to the formation of the Ni_3C phase during carburization.

Thermal annealing of the carbon-incorporated Ni/Si-MCPs is another crucial process for MLG-MCPs formation by the carbon segregation. The Ni_3C phase is known to be unstable at temperatures between 325□ and 480□[34], it completely decomposes into a mixture of nickel phases and graphite phases due to carbon segregation at temperature above 480 ℃[29]. The decomposition equation for Ni_3C in Ar atmosphere should be

$$Ni_3C(s)=3Ni(s) +C(s) \qquad (1)$$
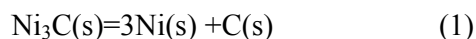
The decomposition of Ni_3C in Ar atmosphere is identified to be a single step reaction. The hexagonal Ni_3C phase peaks of the samples gradually diminished from 300℃ to 400℃， until above 500℃ only cubic Ni phase was detected and all hexagonal phase peaks disappeared, as shown in the XRD patterns in Fig. 5c. At the same times, a trace of a graphite (002) peak at $2\theta=26°$ (marked with pentagram) obviously emerged after thermal annealing at 300℃，whereas no graphite peak was found before annealing (Fig. 5c magenta line). These results were confirmed by the selected area electron diffraction (SAED) patterns (Fig. 4c). These show that the hexagonal phase of Ni_3C before the post-annealing were changed into the cubic phase after the carbon dissociation by the post-annealing.

As shown in Fig. 5d, Raman spectroscopy of the samples using a 633 nm laser after thermal annealing at different temperature revealed three main peaks of graphene (Sample 1: MLG-MCPs 600, annealed 600℃; Sample 2: MLG-MCPs 700, annealed 700℃; Sample 3: MLG-MCPs 800; annealed 800℃). The D (A_{1g}) and G (E_{2g}) bands associated with sp^2 carbon at 1350 cm^{-1} and 1580 cm^{-1}, respectively, indicate the existence of defects in the graphitic lattice and graphitic sp^2-structure. The peak at 2700 cm^{-1} is attributed to the 2D band (two phonons) and assigned to the number of layers of graphene[23]. Moreover, the D and G peaks of samples annealed at under 300 ℃ were obviously weaker than these annealed at above 300 ℃ in Fig. 5d, indicating that graphite phase carbon in $Ni_3C/Ni/Si$-MCPs was segregated and deposited on the after heat treatment at above 300 ℃, which was consistent with the discussion of XRD. As-deposited and annealed MLG at above 500 ℃ showed a apparently larger I_{2D}/I_G ratio (value<1, ~0.2) on Ni/Si-MCP substrates, than that annealed at under 500℃ temperature, indicating extremely high quality and multi-layer graphene for well field emission, which are superior to reduced graphene oxide (rGO) made by modified Hummer's method and then thermal exfoliation.

It is well established that the I_{2D}/I_G ratio increased and the number of graphene layers decreased with the increasing of temperature, and the I_D/I_G ratio value were 0.9, 0.7, 1.0, 1.1, respectively. The I_D/I_G ratio value was lower at the same treated temperature than other report[33]. The decrease in the I_D/I_G ratio from 0.9 to 0.7 shown un-exfoliated graphite phase contained oxygen species of carbon segregated. The increase in the I_D/I_G ratio from 0.7 to 1.1 in MLG/-MCPs indicated a decrease in the

13

average size of the sp2 domains and the removal of the oxygen functional groups from the graphite contained oxide element.   The stronger D peak of samples indicate more defects in MLG-MCPs after post-annealing at high temperature, which will decrease work function of samples to support the well field emission performance.

Further the grain size of graphene was calculated by using I_D/I_G ratio value, according to the following equation.

$$I_D/I_G = C(\lambda)/L_a \qquad (5)$$

Where L_a(nm) is the grain size, λ(nm) is the wavelength of incident light and $C(\lambda)$ is a constant calculated as $C(\lambda) \sim 4.4$ nm[35, 36]. The values of L_a rough calculated via this equation are found to vary from ~4.0nm to ~6.3nm.   These results clearly show that thermal treatment of MLG-MCPs increased their defects, the gaps and sharps as active emission sites, which will increase field emission performance.

The electron-field-emission characteristics of patterned MLG/Ni/Si-MCPs and Ni/Si-MCPs were measured in a chamber with a vacuum of $\sim 2 \times 10^{-5}$ Pa at room temperature (Fig. 6a).   Fig. 6b shows the electron field emission current density (J) versus applied electric field (E) characteristics of the Ni/Si-MCPs, sample 1, sample 2, and sample 3.   The J-E behavior generally follows an exponential relationship of Fowler and Nordheim.   In the simple form, the Fowler-Nordheim (F-N) equation is expressed below[24] assuming that the work functions of graphene and Ni are ~5 eV and ~ 4.5 eV, respectively:

$$J(E) \sim E^2 \exp(-\frac{b\varphi_k^{3/2}}{\beta E}), \qquad (6)$$

where b = 6.83 V $eV^{-3/2}$ nm^{-1} and φ_K and β are the work function and field

14

enhancement factor, respectively.   By plotting ln J/E^2 versus E^{-1}, the F-N plot is

obtained.   In the pure tunneling situation, it should be linear with a slope of

$-b\varphi_k^{3/2}/(\beta E)$ at high electric fields and the F-N plot in Fig. 6(c) indicates that the

observed phenomenon was indeed electron field emission.

Table 1. Key performance Parameters of the graphene Field Emitters Reported in the Literature and   our work to Improve the Field-Emission Properties[a]

field emitters	E_{to}(V/µm)	E_{thr}(V/µm)	β(cm^{-1})	Retention ratio(%)	ref
Graphite sheets	4.7	>6	-	-	41
FLGSs sheets	2.23	4.22	4333	-	40
Patterned rGO nanosheet	3.34	6.7	-	95	25
Well-aligned graphene arrays	7.2	>12	1000	78	27
Aligned graphenes	4.8	5.6	500	79	42
Graphene EPD	4.14	9.4	979	-	43
SnO$_2$	10.0	19.7	496	-	
G-SnO$_2$	5.39	10.2	901	-	
Graphene-silicon nanowire	2.42	3.49	1068	95	26
Graphene-silicon vertices	2.3	3.3	1640	100	44
Graphene/ZnO nanowires	2.4	4.5	5661	-	45
Ni/Si-MCPs	4.3V/um	>6V/um	200	-	our work
MLG-MCPs 600	3.1V/um	4.1V/um	2300	-	
MLG-MCPs 700	2.6V/um	3.6V/um	2500	-	
MLG-MCPs 800	2.0V/um	3.2V/um	3800	97.5	

[a]The turn-on field and threshold field are at current densities of 10µA/cm^2 and 1.0 mA/cm^2,respectively.

The J-E curves show that the turn-on fields of Ni/Si-MCPs, sample 1, sample 2,

and sample 3 were 4.3 V/µm, 3.1 V/µm, 2.6 V/µm, and 2.0 V/µm, respectively.

Sample 3 delivered the best field emission performance with the lowest turn-on field.

According to SEM and Raman scattering, sample 3 had the multi-layer graphene

structure and more exposed graphene edges since it was annealed at the highest

temperature.   More graphene edges produced more emission sites and consequently

higher emission current at the same electric field.   The field-enhancement factor (β)

of patterned sample 1, sample 2 and sample 3 were 2300, 2500, and 3800, respectively, all of which larger than that of Ni/Si-MCPs of 200. The current stability is another crucial factor in FED application. The field-emission current density of sample 3 was measured at a mean J of 2.43 mA/cm^2 for a period of 6 h and stable field emission with 97.5% retention was observed (Fig. 6d). The excellent FE stability arises from the uniform 3D structure of the patterned and porous MLG/Ni/Si-MCPs,enabling fast heat dispersion and lessening the effects of Joule heating on reduction of effective emission sites [25].

For comparison, Table 1 shows that key performance parameters of the graphene field emitters reported in the literature and our work to improve the field-emission properties. It can be seen that field emission of our MLG-MCPs is also improved largely by hydrothermal carbonization. We found that the E_{to} value of MLG-MCPs 800 was lower than reported patterned graphene and metal oxide/graphene composites. Because of porous MLG-MCPs, the stability of sample 3 was better than patterned graphene and metal oxide decorated graphene at a mean J of 2.43 mA/cm^2 for a period of 6 h. So, MLG-MCPs as field emission cathode can effectively improve the field emission properties of MLG.

The distribution of electric potential and electric field of MLG-MCPs and Ni/Si-MCPs were simulated in the Ansys (V. 15.0) environment in Fig. 7a, b, c and d, respectively. Potential distributions were estimated by the method of a finite difference route. Electric filed gradients were calculated using the Forth Runge Kutta formalism. Under the simulations, the distance between electrodes (d) was remained

16

~10 μm, and V$_{anode}$ is 40 V. The thickness and depth of samples was 1 μm and 250 μm, respectively.   The electric potential difference of MLG-MCPs between anode and cathode was stronger than that of Ni/Si-MCPs, which led to difficult move of electric from cathode to anode at Ni/Si-MCPs, decreasing the electron current density of field emission at the sample of Ni/Si-MCPs.   As shown in Fig. 7b and d, due to the positive correlation relationship between electric field and current density,   so current density of MLG-MCPs were dramatically stronger than that of Ni/Si-MCPs, which contributed to multilayer graphene coated Ni/Si-MCPs with lower work function and special electrical performance.

The excellent field-emission properties of the MLG-MCPs emitter can be explained as follows, as shown in Fig.8.   First of all, the multi-layer graphene on MLG-MCPs has a nano-thickness, large aspect ratio, excellent electrical conductivity, and good mechanical properties, all of which are required attributes of an excellent field emitter.   Secondly, the vertically aligned and patterned multi-layer graphene has sharp edges and surface defects to form a distorted sp^3-hybrided geometry instead of the planar sp^2-hybridized configuration.   The porous MLG-MCPs have many surface states arising from surface defects to increase the surface potential barrier and reduce the work function.   It is noted that these results are consistent with previous reports on CNTs and graphene[10,16].   Thirdly, the multi-layer graphene fabricated by hydrothermal carburization has electron channel length of 250 μm thus giving rise to a large current density.   Fourthly, the interface contact and adhesion between the multi-layer graphene and Ni/Si-MCPs are good because of carbon has a high solid

solubility in Ni thus improving the stability. Last but not least, the uniform 3D structure of the patterned and macro porous MLG-MCPs enables faster heat dispersion and reduces the effects of Joule heating on the effective emission sites.

4. Conclusions

In Summary, multi-layer graphene was deposited on Ni/Si-MCPs by hydrothermal carburization and annealing. The structure had sharp edges, large aspect ratio and the vertically and horizontally aligned and patterned multi-layer graphene with good electrical conductivity delivered excellent field-emission performance and stability boding well for application to display and sensing. The process to produce the MLG-MCPs is simple, low-cost, and environmentally friendly and can be readily scaled up for industrial production.

Acknowledgements

References:

1.	B. Hu, K. Wang, L. H. Wu, S. H. Yu, M. Antonietti and M. M. Titirici, *Adv. Mater.*, 2010, **22**, 813-828.

2.   H. W. Kroto, J. R. Heath, S. C. O'Brien, R. F. Curl and R. E. Smalley, *Nature*, 1985, **318**, 162-163.

3.   S. Iijima, *nature*, 1991, **354**, 56-58.

4.   K. S. Novoselov, A. K. Geim, S. Morozov, D. Jiang, Y. Zhang, S. Dubonos, I. Grigorieva and A. Firsov, *science*, 2004, **306**, 666-669.

5.   S.-H. Yu, X. Cui, L. Li, K. Li, B. Yu, M. Antonietti and H. Cölfen, *Adv. Mater.*, 2004, **16**, 1636-1640.

6.   Z.-S. Wu, G. Zhou, L.-C. Yin, W. Ren, F. Li and H.-M. Cheng, *Nano Energy*, 2012, **1**, 107-131.

7.   M. Sookhakian, Y. Amin, S. Baradaran, M. Tajabadi, A. M. Golsheikh and W. Basirun, *Thin Solid Films*, 2014, **552**, 204-211.

8.   S. Basu and P. Bhattacharyya, *Sensor. Actuat. B-Chem.*, 2012, **173**, 1-21.

9.   W. A. De Heer, A. Chatelain and D. Ugarte, *Science*, 1995, **270**, 1179-1180.

10.   S. Fan, M. G. Chapline, N. R. Franklin, T. W. Tombler, A. M. Cassell and H. Dai, *Science*, 1999, **283**, 512-514.

11.   Z. S. Wu, S. Pei, W. Ren, D. Tang, L. Gao, B. Liu, F. Li, C. Liu and H. M. Cheng, *Adv. Mater.*, 2009, **21**, 1756-1760.

12.   W.-C. Shih, J.-M. Jeng, M.-H. Tsai and J.-T. Lo, *Appl. Surf. Sci.*, 2009, **255**, 7679-7682.

13.   W. Lei, C. Li, M. T. Cole, K. Qu, S. Ding, Y. Zhang, J. H. Warner, X. Zhang, B. Wang and W. I. Milne, *Carbon*, 2013, **56**, 255-263.

14.   J. Du, Y. Zhang, S. Deng, N. Xu, Z. Xiao, J. She, Z. Wu and H. Cheng, *Carbon*, 2013, **61**, 507-514.

15.   L. Zhang, X. Liu, Z. Lian, X. Wang, G. Shen, D. Shen and Q. Yan, *J. Mater. Chem. C*, 2014, **2**, 3965-3971.

16.   R. R. Devarapalli, R. V. Kashid, A. B. Deshmukh, P. Sharma, M. R. Das, M. A. More and M. V. Shelke, *J. Mater. Chem. C*, 2013, **1**, 5040-5046.

17.   J. Li, J. Chen, B. Shen, X. Yan and Q. Xue, *Appl. Phys. Lett.*, 2011, **99**, 163103.

18.   P. Hojati-Talemi and G. P. Simon, *Carbon*, 2011, **49**, 2875-2877.

19.   S. Wang, H. Tian, Q. Meng, C. Zhao, L. Qiao, Y. Bing, C. Hu, W. Zheng and Y. Liu, *Appl. Surf. Sci.*, 2012, **258**, 6930-6937.

20.   K. Teii and M. Nakashima, *Appl. Phys. Lett.*, 2010, **96**, 023112.

21.   M. Qian, T. Feng, H. Ding, L. Lin, H. Li, Y. Chen and Z. Sun, *Nanotechnology*, 2009, **20**, 425702.

22.   J. Xu, R. Pan, Y. Chen, X. Piao, M. Qian, T. Feng and Z. Sun, *J. Alloy. Compd.*, 2013, **551**, 348-351.

23.   W. Zhou, S. Xue, J. Han and P. Xie, *Mater. Lett.*, 2014, **134**, 256-258.

24.   S. Wu, S. Xue, Y. Zeng, W. Zhou and J. Han, *Appl. Phys. Express.*, 2014, **7**, 095101.

25.   Y. Peng and D. Huang, *Applied Surface Science*, 2013, **283**, 81-86.

26.   J.-H. Deng, L. Cheng, F.-J. Wang, D.-J. Li and G.-A. Cheng, *Mater. Lett.*, 2015, **138**, 175-178.

27.   C.-K. Huang, Y. Ou, Y. Bie, Q. Zhao and D. Yu, *Applied Physics Letters*, 2011, **98**, 263104.

28.   J. Wu, Y. Zhang, B. Wang, F. Yi, S. Deng, N. Xu and J. Chen, *Nuclear Instruments and Methods in Physics Research Section B: Beam Interactions with Materials and Atoms*, 2013, **304**, 49-56.

29.   G. J. Kovács, I. Bertóti and G. Radnóczi, *Thin Solid Films*, 2008, **516**, 7942-7946.

30. M. Bonder, E. Kirkpatrick, T. Martin, S.-J. Kim, R. Rieke and D. L. Leslie-Pelecky, *J. Magn. Magn. Mater*, 2000, **222**, 70-78.

31. J.-B. Wu, X. Zhang, M. Ijäs, W.-P. Han, X.-F. Qiao, X.-L. Li, D.-S. Jiang, A. C. Ferrari and P.-H. Tan, *Nat. Commun.*, 2014, **5**.

32. Q. Yu, J. Lian, S. Siriponglert, H. Li, Y. P. Chen and S.-S. Pei, *Appl. Phys. Lett.*, 2008, **93**, 113103.

33. S.-M. Yoon, W. M. Choi, H. Baik, H.-J. Shin, I. Song, M.-S. Kwon, J. J. Bae, H. Kim, Y. H. Lee and J.-Y. Choi, *ACS nano*, 2012, **6**, 6803-6811.

34. Y. Leng, L. Xie, F. Liao, J. Zheng and X. Li, *Thermochim. Acta*, 2008, **473**, 14-18.

35. S. J. Chae, F. Güneş, K. K. Kim, E. S. Kim, G. H. Han, S. M. Kim, H. J. Shin, S. M. Yoon, J. Y. Choi and M. H. Park, *Adv. Mater.*, 2009, **21**, 2328-2333.

36. F. Tuinstra and J. L. Koenig, *J. Chem. Phys.*, 1970, **53**, 1126-1130.

37. K. A. Dean, T. P. Burgin and B. R. Chalamala, *Appl. Phys. Lett.*, 2001, **79**, 1873-1875.

38. M. Li, S. Xu, T. Liu, F. Wang, P. Yang, L. Wang and P. K. Chu, *J. Mater. Chem. A*, 2013, **1**, 532-540.

39. F. Miao, B. Tao, L. Sun, T. Liu, J. You, L. Wang and P. K. Chu, *J. Power. Sources.*, 2010, **195**, 146-150.

40. J. Qi, X. Wang, W. Zheng, H. Tian, C. Hu and Y. Peng, *Journal of Physics D: Applied Physics*, 2010, **43**, 055302.

41. J. Wang, M. Zhu, R. Outlaw, X. Zhao, D. Manos, B. Holloway and V. Mammana, *Appl. Phys. Lett.*, 2004, **85**, 1265-1267.

42. J. Chen, L. Cui, D. Sun, B. Yang, J. Yang and X. Yan, *Appl. Phys. Lett.*, 2014, **105**, 213111.

43. J. Ding, X. Yan, J. Li, B. Shen, J. Yang, J. Chen and Q. Xue, *Acs. Appl. Mater. Inter.*, 2011, **3**, 4299-4305.

44. E. Stratakis, G. Eda, H. Yamaguchi, E. Kymakis, C. Fotakis and M. Chhowalla, *Nanoscale*, 2012, **4**, 3069-3074.

45. J. O. Hwang, D. H. Lee, J. Y. Kim, T. H. Han, B. H. Kim, M. Park, K. No and S. O. Kim, *J. Mater. Chem.*, 2011, **21**, 3432-3437.

46. L. Wang, C. Liang, S. Xu and Y. Zhu, Chinese Patent Pending No. 2015101249340
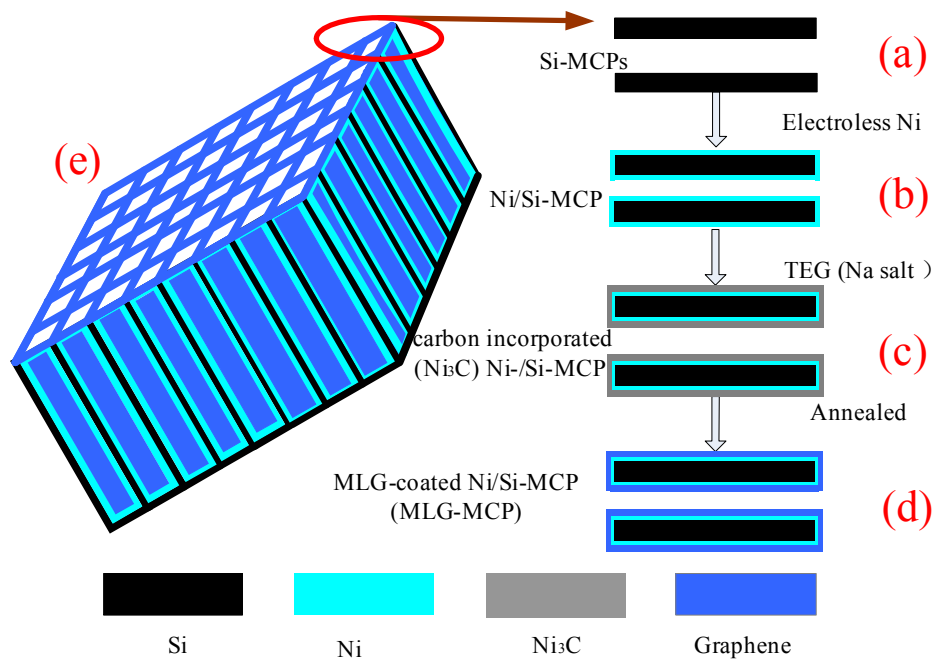
Fig. 1. Schematic illustrating the synthesis procedure of multi-layer grapheme (MLG) -coated Ni/Si-MCP(MLG-MCPs): (a) Si-MCP; (b) Ni/Si-MCP; (c) Carbon-incorporated Ni (Ni_3C)/Si-MCP; (d) Single MLG-MCP; (e) MLG-MCPs.
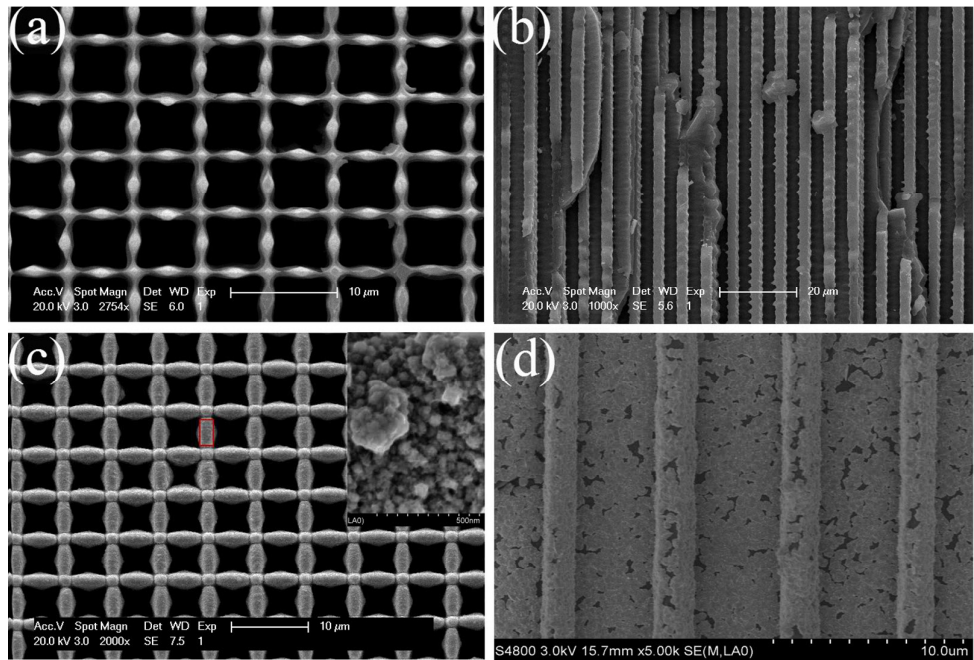

Fig. 2. SEM images: (a) Top surface of Si-MCPs. (b) Cross-sectional morphology of a. (c) Top surface of Ni/Si-MCPs with the inset showing the magnified selected area of Ni/Si-MCPs. (d) Cross-sectional morphology of the Ni/Si-MCPs.
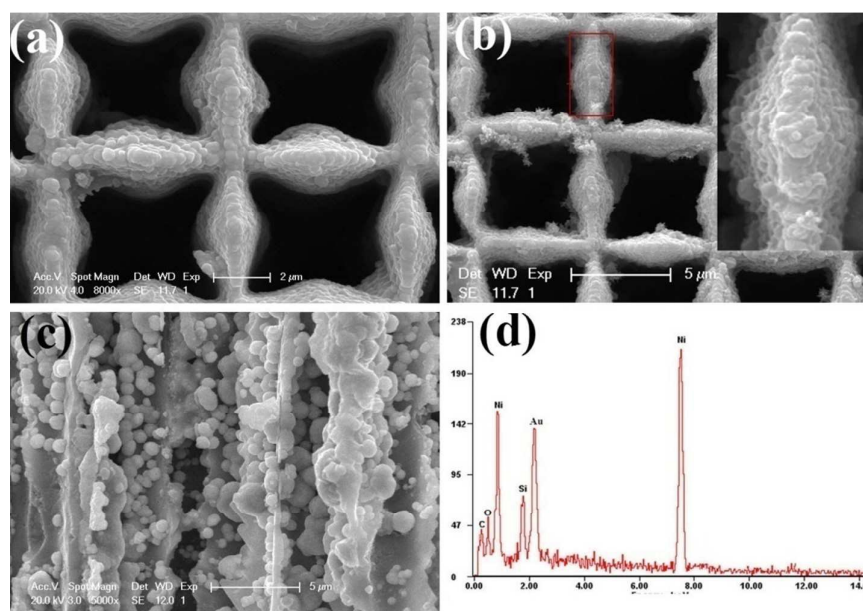
1

Fig. 3. SEM image: (a) Top view of carbon-incorporated Ni nano-sheets (Ni$_3$C)/Si-MCP.
(b) Top view of MLG-MCPs with the inset showing the magnified selected area of MLG-MCPs.
(c) Cross-sectional morphology of MLG-MCPs. (d) EDX picture of MLG-MCPs.
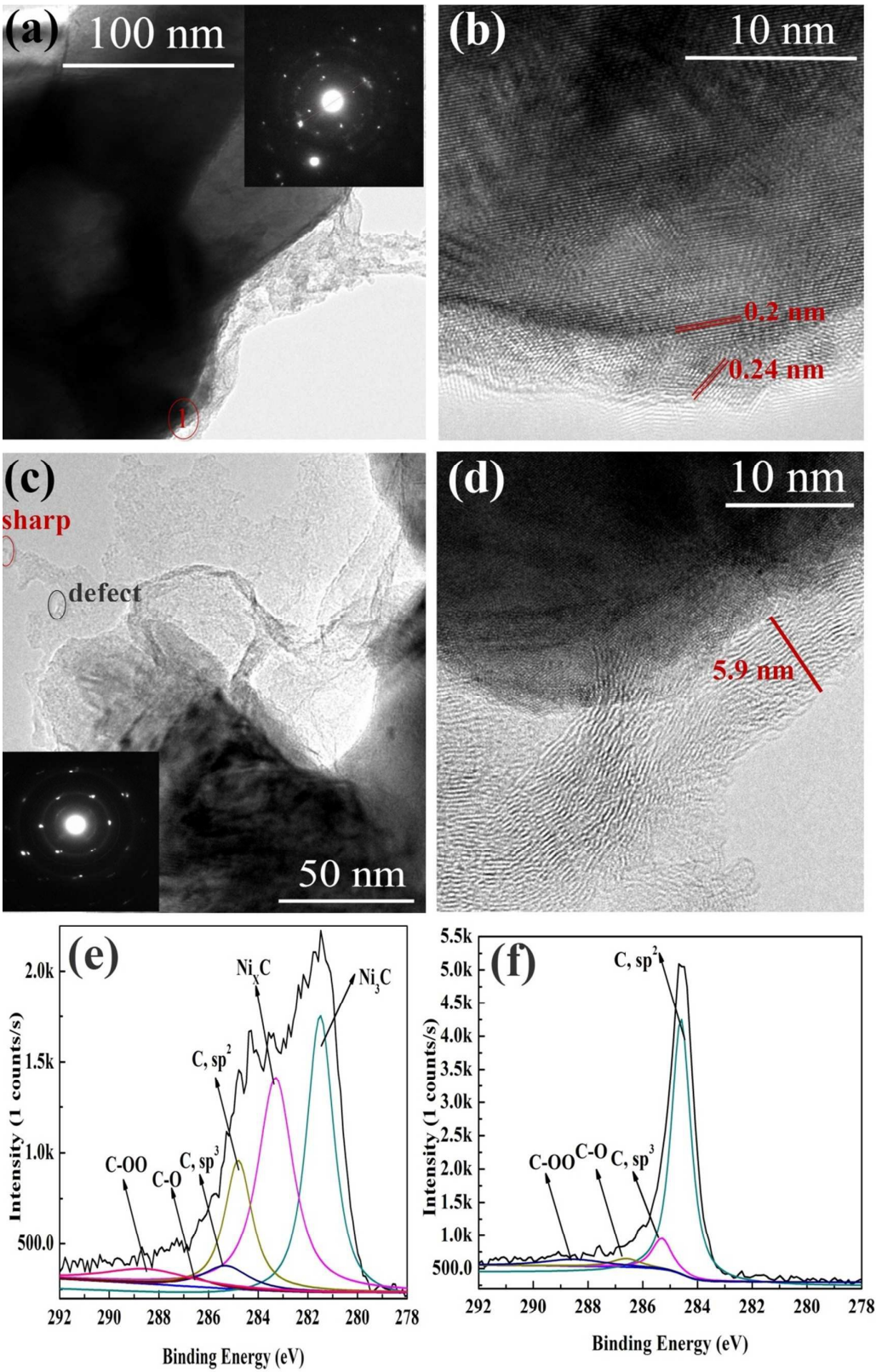
Fig. 4. (a) TEM image of Ni$_3$C/Ni composites (insets: SAED pattern of area 1 region).   (b) HR-TEM image of Ni$_3$C/Ni composites of area 1 region in (a).   (c) TEM image of MLG/Ni

composites (insets: SAED pattern of transparent region).   (d) HR-TEM image of MLG/Ni composites.   (e) The C 1s peak envelope of Ni_3C/Ni composites.   (f) The C 1s peak envelope of MLG/Ni composites annealed at 800℃.
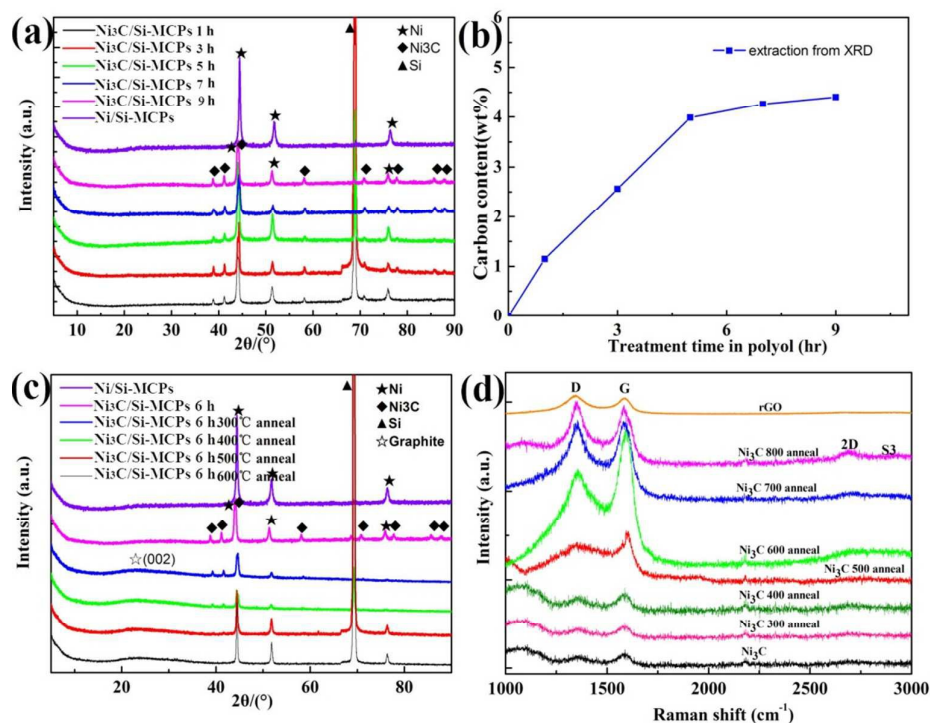

Fig. 5   XRD and Raman: (a) XRD of the carbon-incorporated (Ni_3C) Ni/Si-MCP obtained after various hydrothermal carburization times in organic solution and starting Ni/Si-MCPs (top). (b) Carbon content of the carbon-incorporated (Ni_3C) Ni/Si-MCPs as a function of the hydrothermal time.   (c) X-ray diffraction patterns of the carbon-incorporated (Ni_3C) Ni/Si-MCP obtained after various thermal annealed temperature in Ar atmosphere.   (d) Raman image of the carbon-incorporated (Ni_3C) Ni/Si-MCP obtained after various thermal annealed temperature in Ar atmosphere.
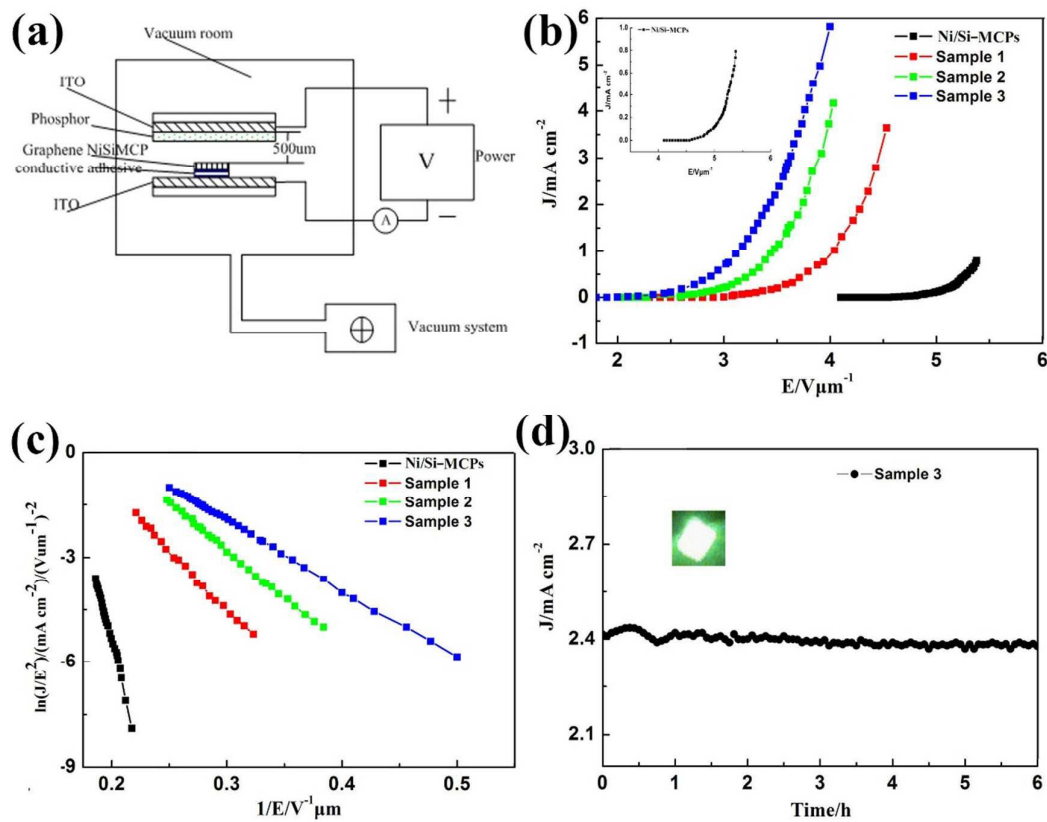
4

Fig. 6 (a) A schematic set up of electron- field-emission from MLG-MCPs. (b) J-E curves of Ni/Si-MCPs as well as samples 1, 2, and 3 (inset image: the data are plotted as J/E for Ni/Si-MCPs). (c) FN plot of Ni/Si-MCPs as well as samples 1, 2, and 3. (d) Emission current stability of sample 3 for 6 h, and the inset shows optical micrographs of sample 3 electron emission display.
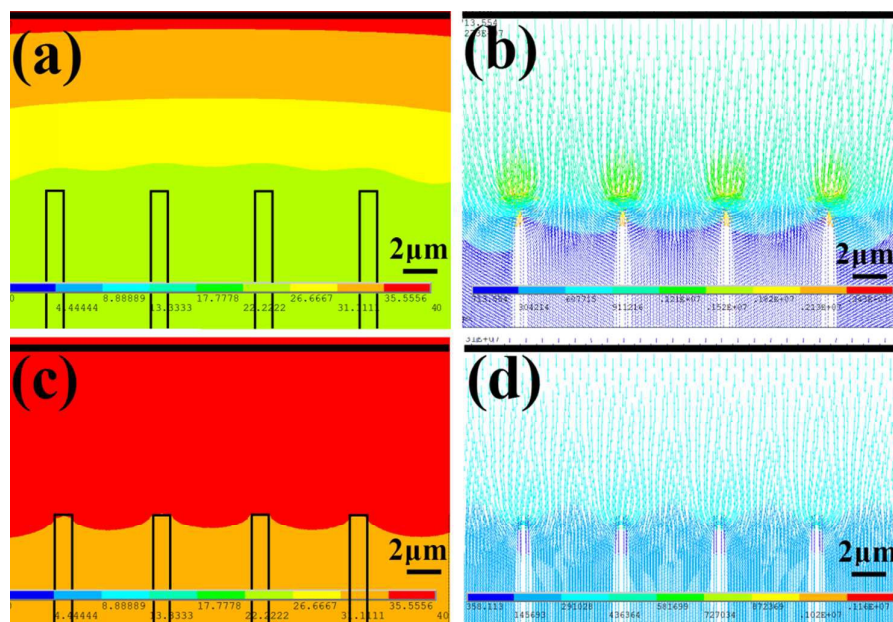
Fig. 7.   (a) and (b) Simulated potential distribution (colar bar, V) and electric field (blue curves, E) at the MLG/Ni/Si-MCPs.   (c) and (d) Image of simulated potential distribution (colar bar, V) and electric field (blue curves, E) at the Ni/Si-MCPs.
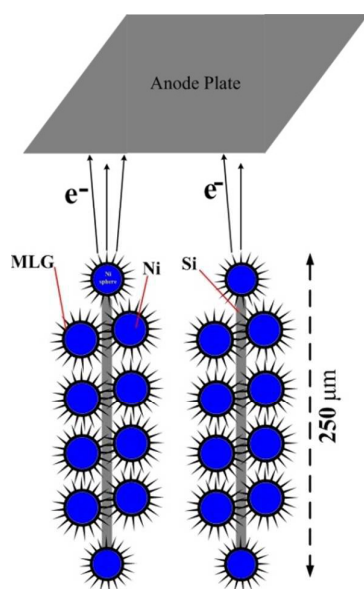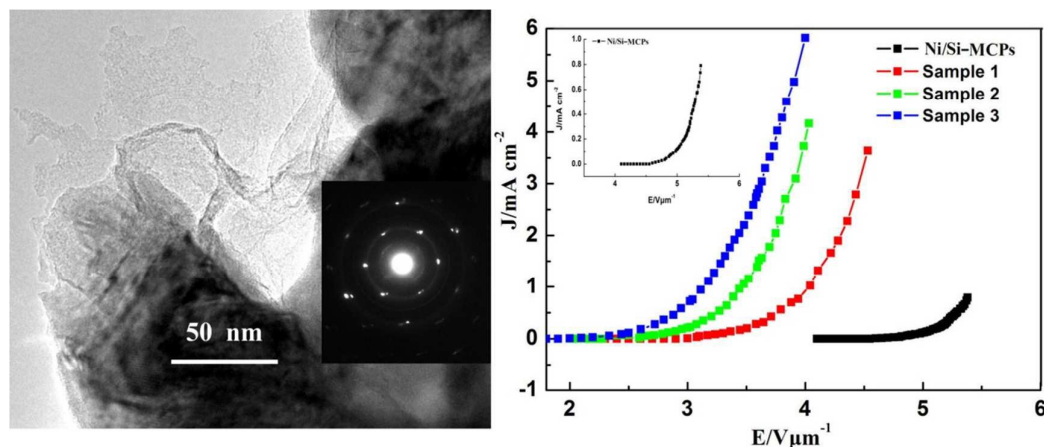

Fig. 8. A schematic diagram showing electron field emission

Graphical Abstract:

An emission cell comprising multi-layer graphene (MLG) on nickel-coated silicon microchannel plates (Ni/Si-MCPs) was prepared. The Ni_3C film was formed on the Si-MCPs by hydrothermal carburization in a polyol solution containing a small amount of NaAc as the carbon source and thermal annealing was performed to produce the vertically and horizontally aligned multi-layer graphene field-emission cathode on the surface of the Ni/Si-MCPs (MLG-MCPs). The microstructure and surface morphology was investigated and field emission (FE) studies indicated that the MLG-MCPs delivered better FE performance than Ni/Si-MCPs, which contributed to the characteristic of had sharp edges, large aspect ratio, and the vertically and horizontally aligned and patterned MLG with good electrical conductivity. The turn-on field of the sample annealed at 800 ^{o}C was 2.0 V/μm at a current density of 10 μA/cm^2 and the field emission threshold was 3.2 V/μm at 1 mA/cm^2. The structure was very stable showing 97.5% retention after continuous operation for over 6 h at 2×10^{-5} Pa, suggesting a promising candidate for FE devices. This would open up possibilities for the next generation FE electron sources from

well-aligned macroporous graphene with skeleton and extend their practical

applications.